Princeton Plasma Physics Laboratory

The ITER 3D magnetic diagnostic response to applied n=3 and n=4 RMP's

S.A. Lazerson

June 2014

PRINCETON
PLASMA PHYSICS
LABORATORY

Princeton Plasma Physics Laboratory
Report Disclaimers

PPPL Report Availability

Princeton Plasma Physics Laboratory:

http://www.pppl.gov/techreports.cfm

Office of Scientific and Technical Information (OSTI):

http://www.osti.gov/bridge

Related Links:

U.S. Department of Energy

Office of Scientific and Technical Information

Fusion Links

The ITER 3D magnetic diagnostic response to applied n=3 and n=4 RMP's ‡

S. A. Lazerson

Princeton Plasma Physics Laboratory, Princeton, NJ

E-mail: `lazerson@pppl.gov`

Abstract. The ITER magnetic diagnostic response to applied n=3 and n=4 RMPs has been calculated for the 15MA scenario. The VMEC code was utilized to calculate free boundary 3D ideal MHD equilibria, where the non-stellarator symmetric terms were included in the calculation [1]. This allows an assessment to be made of the possible boundary displacements due to RMP application in ITER. As the VMEC code assumes a continuous set of nested flux surface, the possibility of island and stochastic region formation is ignored. At the start of the current flat-top (L-Mode) application of $n = 4$ RMP's indicates approximately 1 cm peak-to-peak displacements on the low field side of the plasma while later in the shot (H-mode) perturbations as large as 3 cm are present. Forward modeling of the ITER magnetic diagnostics indicates significant non-axisymmetric plasma response, exceeding 10% the axisymmetric signal in many of the flux loops. Magnetic field probes seem to indicate a greater robustness to 3D effects but still indicate large sensitivities to 3D effects in a number of sensors. Forward modeling of the diagnostics response to 3D equilibria allows assessment of diagnostics design and control scenarios.

1. Introduction

The ITER device must be able to suppress edge localized modes (ELMs), as the heat flux associated with such phenomena are not tolerable [2]. One method to achieve such suppression is through the application of resonant magnetic perturbations (RMPs) via a set of 3D in-vessel magnetic coils (Figure 1). The effect of the n=3 and n=4 resonant magnetic perturbations on the ITER plasma have received much treatment in literature [3, 4]. In a pervious paper, the authors calculated the diagnostic response of an ITER 15MA H-mode plasma to an applied n=3 RMP [5]. In that paper, a trial set of magnetic diagnostics were placed on the first wall surface, as at the time the full diagnostic set was not available. The designed magnetic diagnostic set [6] is now considered along with refined and expanded transport modeling [7]. Such modeling was utilized to determine equilibrium pressure and current profiles.
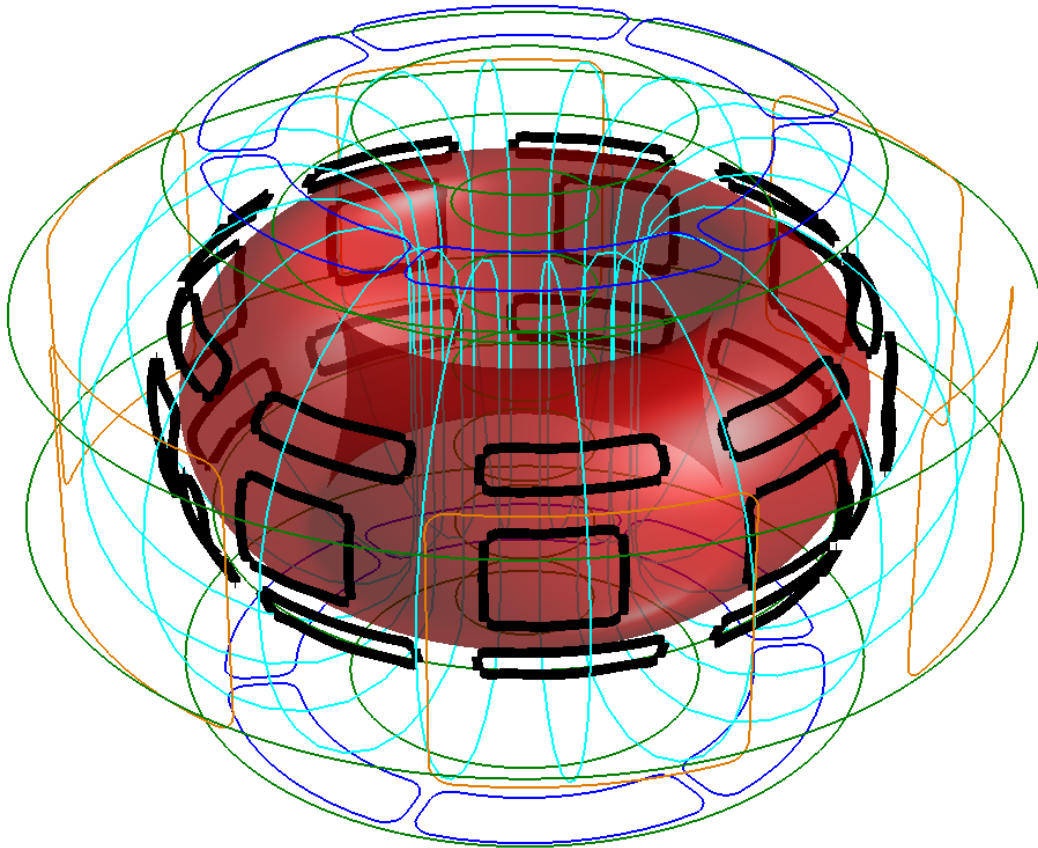
Figure 1. The ITER coil set with in-vessel coils highlighted (thick black). A VMEC axisymmetric equilibria is depicted for reference. Single current filaments are depicted for clarity while the full multi-filament coil set is utilized in all calculations.

In this work the ITER 15MA scenario is examined for both an L-Mode and H-Mode plasma with applied RMPs. Transport modeling of the scenario provides equilibrium profile data early in the shot just after the current flat top (L-Mode) and once the

plasma reaches full burn (H-Mode, 3 [keV] pedestal). Such modeling provides current and pressure profiles for the VMEC 3D equilibrium code. The plasma response to an applied n=3 RMP (at peak coil current of 45 [kA-t] and 90 [kA-t]) and n=4 RMP (at peak coil current of 30 [kA-t] and 90 [kA-t]) are calculated as well as the unperturbed equilibrium configurations. This provides 10 equilibria which are considered (8 with 3D character and 2 in axisymmetry). It should be noted that 90 [kA-t] is the maximum designed current carrying capability of the ITER in-vessel coils. The magnetic diagnostic response is then calculated for each of these scenarios. The next section discusses the equilibria generated, followed by a section discussing the diagnostic response. The final section discusses the results and future work.

2. Equilibrium Calculations

The VMEC code was utilized to calculate the free boundary 3D ideal MHD ITER equilibria. In order to assure consistency with transport modeling, VMEC was utilized to calculate 2D free boundary equilibria which were then matched to the 2D transport simulations preformed by the CORSICA code [8]. Once axisymmetric 2D equilibria were generated using VMEC, free boundary calculations with the I-coils energized were calculated. This method neglects the transport response due to RMP application.
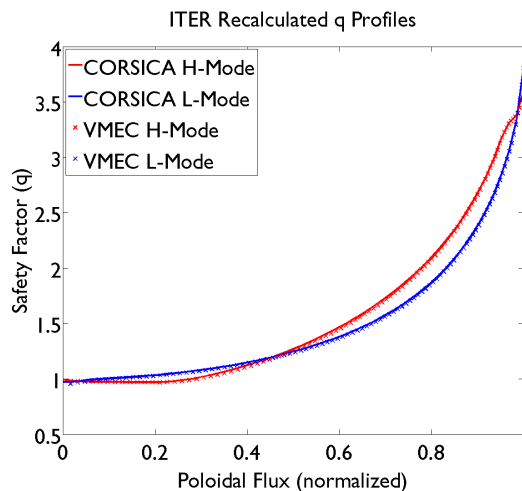
Figure 2. Comparison between the axisymmetric VMEC (x) and CORSICA (-) q profiles. The VMEC calculations at fixed current profile agree with the CORSICA calculations for q.

The STELLOPT code [9] was utilized to match the axisymmetric VMEC equilibrium to those produced by the CORSICA code. The enclosed toroidal flux, net toroidal current, pressure scaling factor, and axisymmetric tokamak coil currents were the varied quantities. The equilibria were then fit to the separatrix provided by CORSICA. Tokamak coil currents were also imposed as a constraint to avoid pathological choices of coil current (coil currents which give a good fit to the separatrix

but are not consistent with the modeled parameters). The current density profile (I') and pressure profile were held fixed to the CORSICA simulation values. Figure 2 depicts the resulting VMEC and CORSICA q profiles. The agreement is good with discrepancies, near the divertor x-point, attributed to the inverse representation of the VMEC code (poloidal modes $0 - 23$).
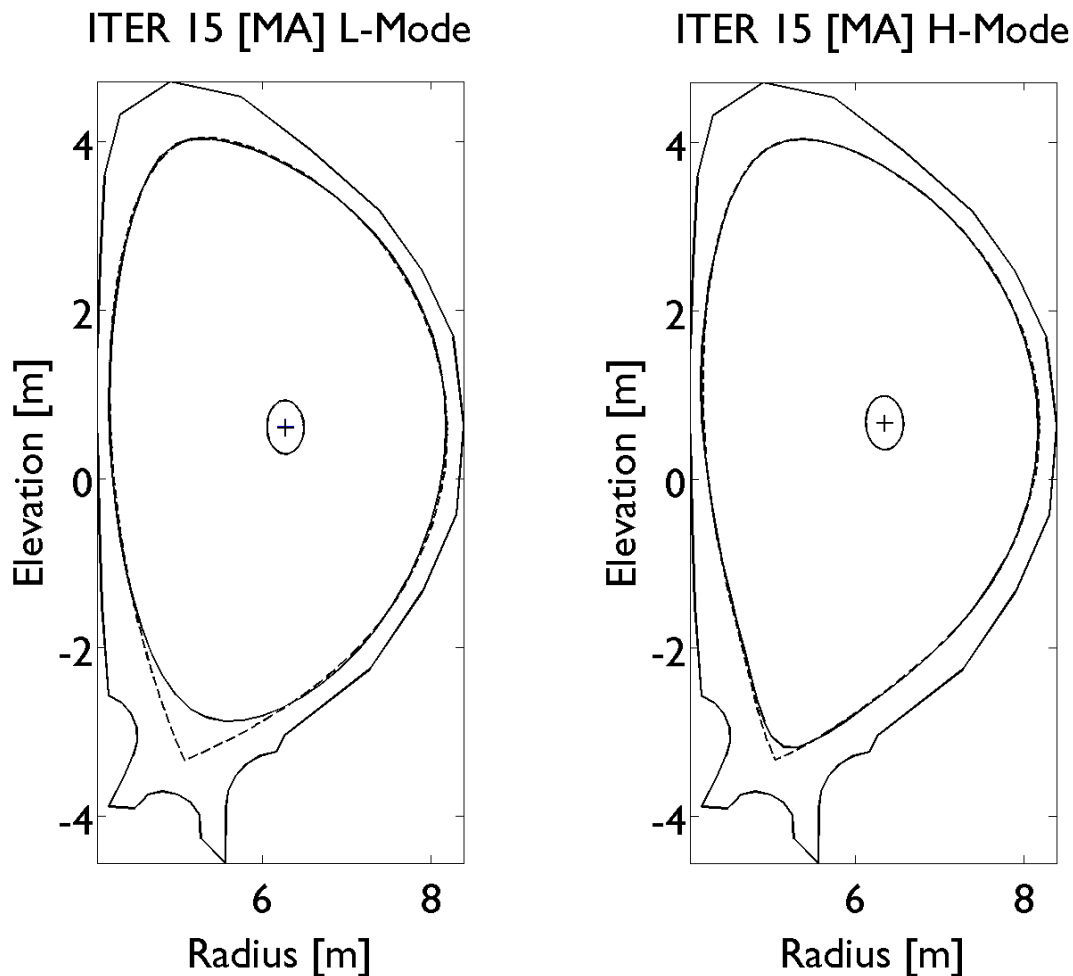
Figure 3. Comparison between the CORSICA separatrix (dashed) and the VMEC edge (solid) for the L-Mode (left) and H-mode (right) scenarios. The CORSICA magnetic axis (+) and VMEC inner most flux surface (solid) are plotted indicating consistency on the axis location. The first wall surfaces are plotted for reference.

Figure 3 depicts the VMEC edge and CORSICA separatrix. The truncation error associated with the finite poloidal mode spectrum exhibits itself as an inability to resolve the diverter x-point in axisymmetry. This is an inherent limit of the inverse representation utilized in the VMEC code. It should be noted that an x-point will still exist outside the inverse representation in the vacuum region. However, the plasma response between the x-point and inverse equilibrium boundary will be missing. The discrepancy between the equilibria becomes less clear in 3D as the x-point should vanish and become surrounded by stochastic field line trajectories. It is argued that agreement

with the axisymmetric boundary away from the x-point is more critical than having a VMEC boundary which passes through the x-point.

Figure 4. Boundary displacement for the ITER L-mode (left) and H-mode (right) scenarios with a $n = 4$ perturbation and 90 $[kA - t]$ of maximum coil current. Upper plots depict boundary displacements in the $\phi = 0$ plane amplified by a factor of 20. This places and upper limit on boundary displacements for this scenario.
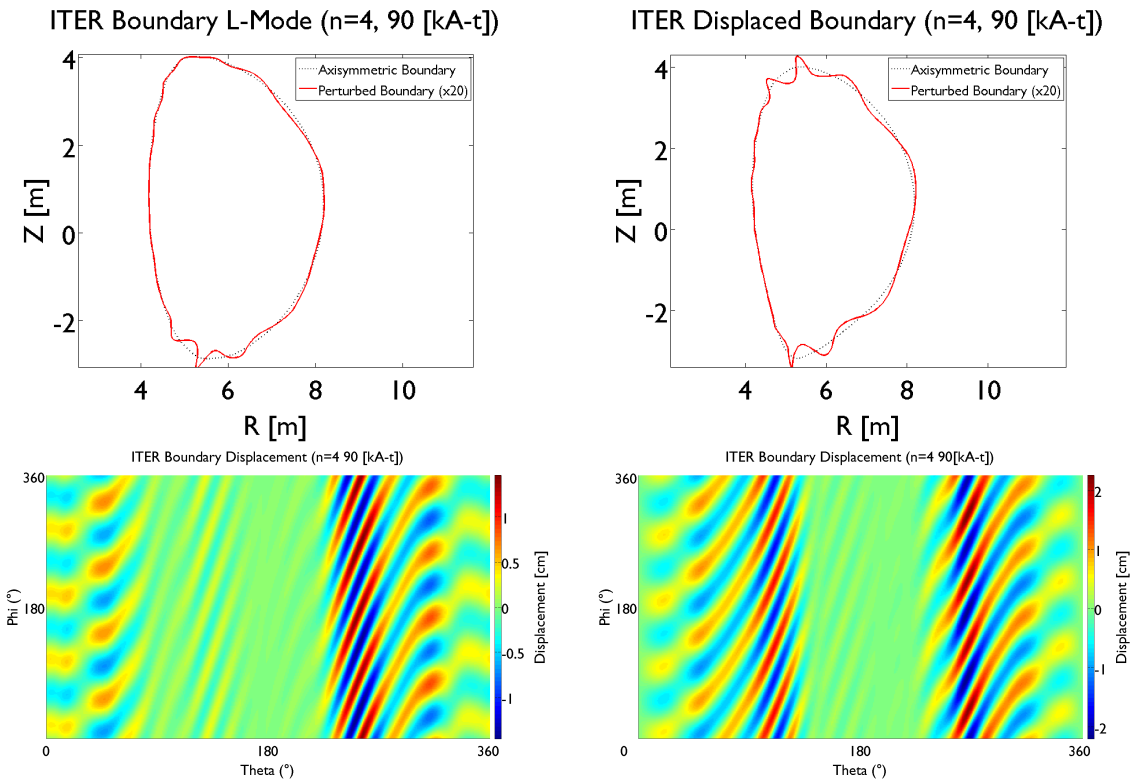
The effect of applied RMPs on the VMEC equilibria was evaluated through full 3D calculations ($n = 3$ and $n = 4$, at maximum and lower current). The ITER ELM coil currents were chosen to achieve a required level of edge magnetic field perturbation to suppress ELMs according to experiments preformed in DIII-D [4, 10, 11]. The necessary vacuum island overlap parameter for ELM suppression was determined by experiments in DIII-D. Vacuum island overlap calculations in ITER were then performed. These perturbations are chosen so that island overlap is maximum in the pedestal region ($q \sim 3$). High n perturbations are preferred over low as the relative coupling (edge vs core) is weighted toward the edge. Table 1 contains the coil currents for each scenario. The vacuum field was sampled at 72 toroidal planes and equilibria were limited to toroidal modes $-4...4$. Boundary displacements were calculated by treating the n=0 modes as the reference axisymmetric boundary. This can be considered appropriate as the boundary displacements are small compared to the equilibrium dimensions. Figure 4 depicts the $n = 4$ 90 $[kA - t]$ coil scenario for both the L and H-mode equilibria. Boundary displacements are consistent with toroidal mode spectrum, and can be as

large as 1.5 [*cm*] in the upper half plane with larger displacements near the diverter region. Table 2 indicates the amplitudes of the boundary displacement for all coil scenarios. The strong response near $\theta = 270^o$ is associated with the diverter x-point and here the VMEC nested flux surface assumption is most likely inappropriate. The amplitude of the boundary displacements appears to scale linearly although more than 3 data points (zero, mid and high coil current) would be necessary to better validate this statement. It should also be noted that the up-down asymmetry in the boundary displacements can be associated with the relatively stronger coil currents in the lower row of coils as compared with upper coil for this scenario (see table 1).

3. Magnetic Diagnostic Response
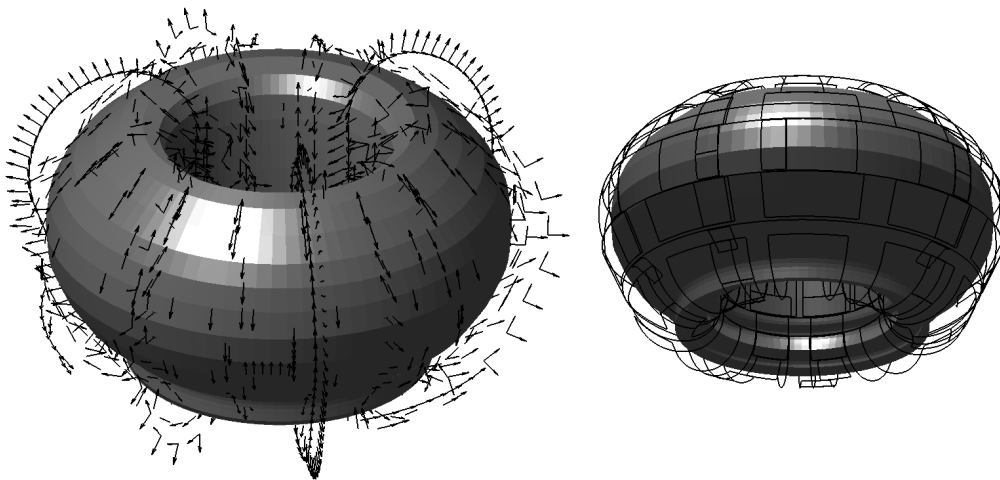
Figure 5. The ITER magnetic field probes (left) and flux loops (right). Here the ITER first wall surface has been depicted for reference (grey).

The DIAGNO2 code [13] was utilized to calculate the magnetic diagnostic response of the designed ITER flux loops and B-field probes (Figure 5). This code employs a virtual casing principle to calculate the plasma response outside the VMEC equilibrium [14, 15], while the vacuum fields were provided by direct Biot-Savart integration over the full multi-filament coil set [16]. The signals calculated by this code have been utilized for 3D equilibrium reconstruction on the W7-AS [17], LHD [18], and DIII-D devices [19], thus validating the applicability of this model for plasma response in 3D devices. As the ITER coil set is superconducting, the toroidal field coil will most likely be ramped up to full field before magnetic diagnostic data acquisition begins. For this reason, the field due to the TF coil has been ignored in the diagnostic response calculation, while the poloidal field, center stack, and in-vessel coil fields are included. The magnetic diagnostic response has been calculated for each of the scenarios in the previous section. In order to address the effects of 3D fields on the diagnostic response, the axisymmetric

Table 1. ITER in-vessel coil currents for each RMP scenario. Current in units of Amp-turns. [4, 12]

Coil	$n = 3$, 45 $[kA - t]$	$n = 3$, 90 $[kA - t]$	$n = 4$, 30 $[kA - t]$	$n = 4$, 90 $[kA - t]$
Upper 01	-9456.0	-85595	-26488	-72811
Upper 02	-33441	18712	20073	86513
Upper 03	42797	66883	-11238	-89781
Upper 04	-9356.0	-85595	1047.0	82219
Upper 05	-33441	18712	9270.5	-64740
Upper 06	42797	66883	-18469	39453
Upper 07	-9356.0	-85595	25441	-9407.6
Upper 08	-33441	18712	-29344	-21772
Upper 09	42797	66883	29708	50327
Middle 01	45000	90000	30000	90000
Middle 02	-22500	-45000	-28190	-84572
Middle 03	-22500	-45000	22981	68944
Middle 04	45000	90000	-15000	-45000
Middle 05	-22500	-45000	5209.4	15628
Middle 06	-22500	-45000	5209.4	15628
Middle 07	45000	90000	-15000	-45000
Middle 08	-22500	-45000	22981	68944
Middle 09	-22500	-45000	-28190	-84572
Lower 01	-9356.0	-82219	-26488	-84572
Lower 02	42797	72811	29708	68944
Lower 03	-33441	9407.5	-29344	-45000
Lower 04	-9356.0	-82219	25441	15628
Lower 05	42797	72811	-18469	15628
Lower 06	-33441	9407.5	9270.5	-45000
Lower 07	-9356.0	-82219	1047.0	68943
Lower 08	42797	9407.5	-11238	-84572
Lower 09	-33441	-82219	20073	90000

Table 2. Maximum boundary displacement as simulated in the upper half plane of the ITER device (units $[cm]$).

Coil Scenario	L-Mode	H-Mode
$n = 3$, 45 $[kA - t]$	0.56	0.84
$n = 3$, 90 $[kA - t]$	0.78	1.36
$n = 4$, 30 $[kA - t]$	0.23	0.36
$n = 4$, 90 $[kA - t]$	0.69	1.66

response is subtracted from the non-axisymmetric scenario responses. The resulting signals represents a superposition of the plasma response and in-vessel coil fields.
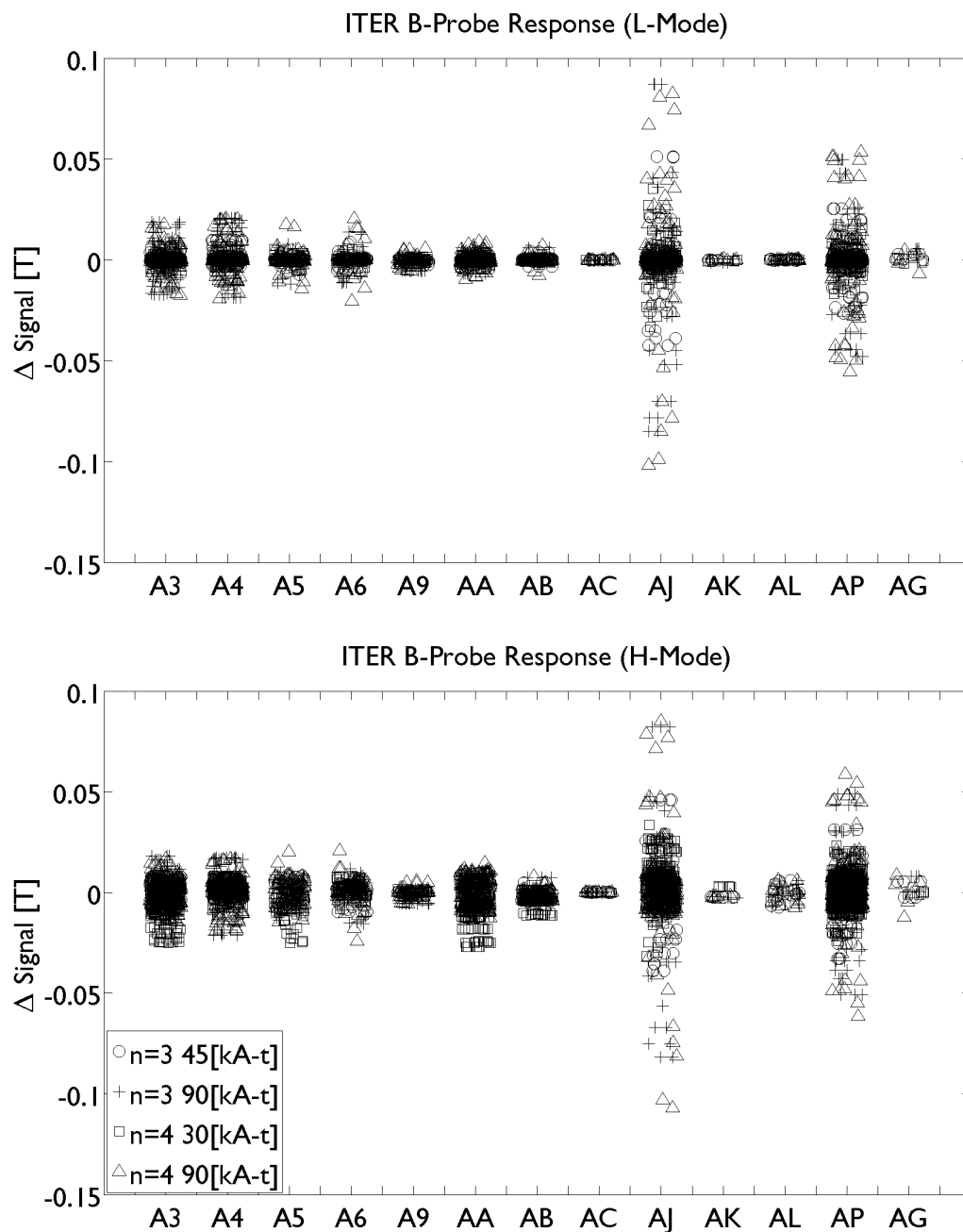
Figure 6. The B-field probe response to applied 3D fields for the ITER L-mode and H-mode cases. Datasets are grouped by probe designation: A3- Tangential Coils, A4- Normal Coils, A5- Tangential Steady State, A6- Normal Steady State, A9- Diamagnetic Compensation, AA- Inner Tangential Coils, AB- Inner Normal Coils, AC- Toroidal Coils, AJ- HF Sensors, AK- RWM Sensors, AL- Divertor Equilibrium, AP- Blanket Rogowski, AG- Inner Diamagnetic Compensation. Horizontal scatter has been artificially added for clarity.

The simulated change in magnetic field probe signals ($\sim$ 1300 probes) are plotted in figure 6 grouped by probe designation. The tangential (A3, A5) and normal coil sets (A4, A6) indicate up to $\sim$ 200 [G] variation associated with the application of 3D fields. Probes located closer to the plasma, such as the high field (AJ) and blanket Rogowski (AP), indicate the strongest variation in signal intensity. Vacuum modeling of the magnetic field probe response suggests that, while coupling to the vacuum field may be present, the majority of the signal is dominated by 3D field response. The largest overall change in response between L and H-mode is detected by the inner tangential coils (AA) and to a lesser extent the inner normal coils (AB). As RMP coil currents were the same between modes, the change in signal for these coils is associated with a 3D change in plasma response.
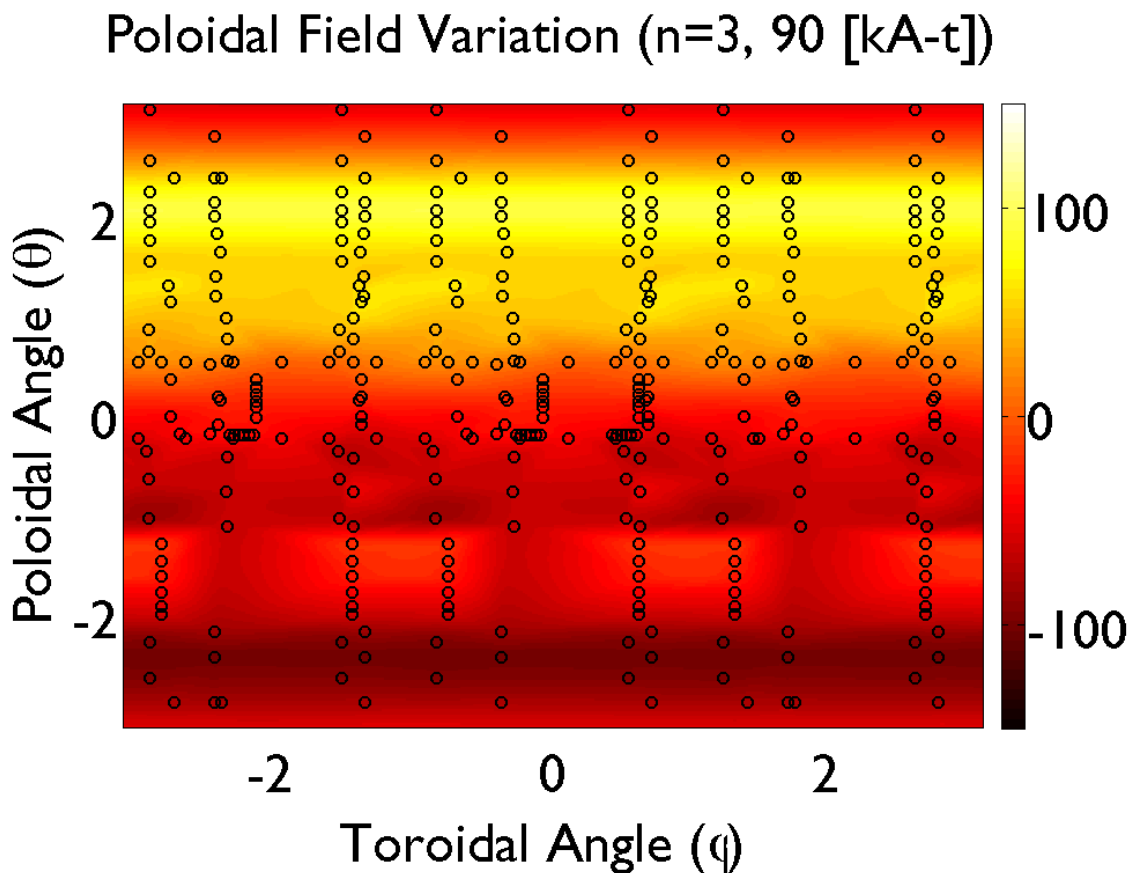
Poloidal Field Variation (n=3, 90 [kA-t])

Figure 7. Interpolation of the poloidal field as simulated by the inner tangential (AA), high field (AJ), and RWM (AK) sensors for the H-mode scenario. The diagnostic response to the vacuum field coils has been subtracted. A clear n=3 feature is present in the simulated response. Sensor locations are plotted for reference (o). The units for the axes are in radians with the outboard mid plane (R=5.3, Z=0) defining the origin.

The magnetic field probe arrays can be utilized to detect the 3D nature of the plasma. Figure 7 depicts the interpolated poloidal magnetic field as simulated by the three sensor arrays closest to the plasma (AA, AJ, and AK). Here the vacuum response

has been subtracted to highlight the ability to detect plasma response. These sensor arrays all lay approximately at the same radial distance from the plasma allowing a relatively simple data interpolation to be preformed. Inclusion of additional sensors, not on the same radial surface, requires more sophisticated data methods for analysis such as 3D equilibrium reconstruction.

It should be noted that generation of toroidal components of the field due to plasma response is possible in the vacuum region if the plasma becomes toroidally distorted (3D). First, consider a perfectly axisymmetric device (ignoring toroidal field ripple and error fields), the poloidal currents in the plasma generate toroidal field inside the plasma but do not generate toroidal field outside the plasma. However, if the boundary begins to deform, in a three dimensional way, toroidal field will be generated by the plasma in the vacuum region (here toroidal refers to the same direction in each instance). Note that the integral of the toroidal field around the torus will remain zero ($\int \vec{B} \cdot \hat{\phi} = 0$). In a real device, the toroidal field due to vacuum effects can be directly measured (toroidal field ripple, error fields, and applied 3D fields) and subtracted from any measured toroidal fields. The resulting variation in the measured toroidal field must be due to 3D effects (and possibly non-axisymmetric eddy currents in the machine). The ITER magnetic field probe set includes nine toroidal magnetic field probes (located at the top of the machine, AC). These coils have a clear capability to detect variations in the plasma response mode number and plasma signals were of the order of 1-2 [G] for the 90 [kA-t] cases in H-mode. In previous work, the utility of additional toroidal field sensors near the low-field side of the plasma was noted [5].
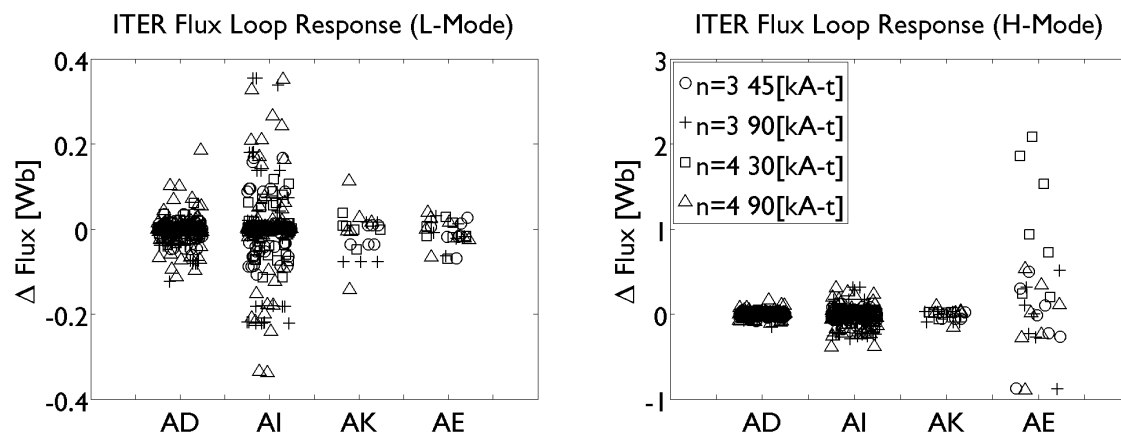

Figure 8. The magnetic diagnostic response attributed to 3D fields for multiple scenarios. Data points are grouped by diagnostic type. Horizontal scatter has been artificially added for clarity: AD- Partial Loops, AI- MHD Saddles, AK- RWM Saddles, AE- Axisymmetric loops.

The flux loop response to 3D fields has been plotted in figure 8. A significant change in response in the axisymmetric flux loops (AE) is present in H-mode. Such large response in the axisymmetric loops was not present for L-mode. This suggests

such a characteristic is due to plasma response, not coupling between the flux loops and the in-vessel coils. Vacuum modeling of the mutual inductances corroborates this conclusion. The variation in signal for the axisymmetric flux loops can vary from a few percent to 40% when compared to the axisymmetric configurations. This is attributed to deformation of the edge currents associated with H-mode. The axisymmetric flux loops simulate the following integral

$$\Phi = \int \vec{A} \cdot \vec{dl} \longrightarrow \int A_\phi R_{loop} d\phi \tag{1}$$

where Φ is the flux through the loop, $\vec{A}$ is the vector potential due to the plasma, $\vec{dl}$ is a differential element along the path of the loop, A_ϕ is the toroidal component of the vector potential, R_{loop} is the major radius of the flux loop, $d\phi$ is a differential element in the toroidal direction, and the arrow indicates transformation to an axisymmetric system. In axisymmetry, the toroidal vector potential (A_ϕ) arrises solely from the toroidal current density (j_ϕ)

$$\vec{A}(\vec{x}) = \int \frac{\vec{j}(\vec{x'})}{\left|\vec{x} - \vec{x'}\right|} dV' \longrightarrow A_\phi(\vec{x}) = \int \frac{j_\phi(\vec{x'})}{\left|\vec{x} - \vec{x'}\right|} dV' \tag{2}$$

where $\vec{j}$ is the current density, $\vec{x}$ is a point in space, and the prime indicates integration over the volume of the current density. As the plasma deforms, the edge bootstrap current will take on a more helical path through space thus changing it's contribution to the toroidal vector potential. Subsequently the axisymmetric flux loop response changes. Unfortunately based on these flux loops alone, it is difficult to differentiate between shifts in plasma position and 3D field effects. The signal from these toroidally symmetric flux loops is clearly modified by the presence of non-axisymmetric plasma structure. However, one could still fit an axisymmetric equilibria to these signals. The result being an equilibrium which may not accurately reflect the true experimental condition. A 3D equilibrium could also be fit to these same signals. Without information regarding toroidal variation of signals, determination of which equilibrium is correct cannot be made.

The saddle type flux loops (non-axisymmetric) posses an ability to constrain the 3D nature of the equilibrium plasma as they simulate both the poloidal and toroidal profile of the radial field. Figure 9 depicts a linear interpolation of the average flux through each saddle type loop. The simulated signals have been treated as flux at the geometric center of each loop (denoted by 'o'). A clear $n = 3$ feature is present along the outboard mid plane ($\theta = 0$). A less pronounce $n = 3$ feature is present near the upper high field side of the plasma ($\theta \sim \pi$). This highlights the capability of these loops to act as constraints to the 3D nature of the plasma.

4. Comments

Three dimensional ideal MHD equilibria for ITER are presented along with their associated magnetic diagnostic response. While the constraint of nested flux surfaces

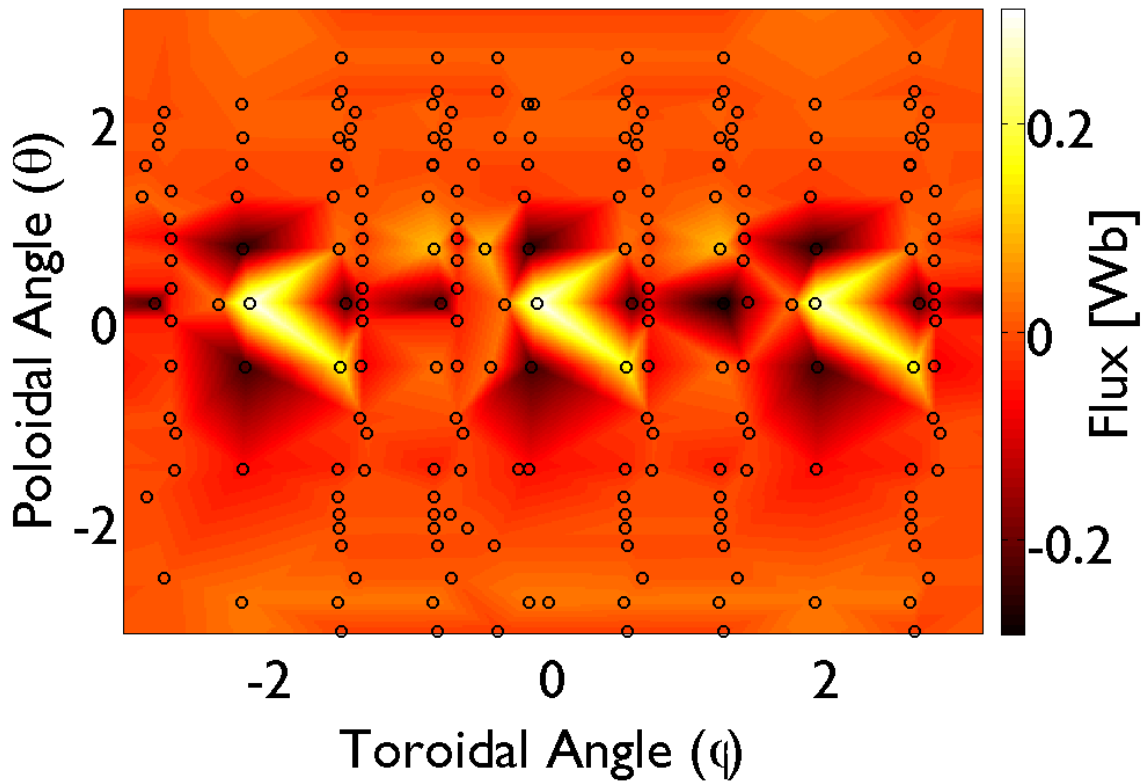## Saddle Loop Response (H-Mode, n=3, 90 [kA-t])

Figure 9. Linear interpolation of the radial magnetic flux as simulated by the non-axisymmetric flux loops in ITER. The geometric center of each loop is denoted (o). A clear n=3 feature is present in the interpolated flux. The axes have units of radians with the outboard mid plane (R=5.3, Z=0) defining the origin.

may be violated locally, the observed boundary displacements are consistent with more sophisticated multi-fluid codes. Near the top of the machine, boundary displacements range from the sub-cm to 3 *cm* (peak-to-peak) which may not be significant, in a plasma wall sense, given the size of the machine and plasma wall gap. However, plasma stability may be greatly affected by such displacements [20]. Such displacements may also be significant to particle orbits at the edge of the plasma, leading to wall loading not predicted by axisymmetric models [21]. Additionally, the effect of islands and stochastic regions have been ignored as the VMEC code is not capable of treating changes to magnetic topology. Assessment of the applicability of VMEC to RMP experiments in tokamaks is an ongoing topic of research [22].

Magnetic diagnostic responses indicate that as resonant fields are applied to the plasma, non-axisymmetric fields are detected along with modifications to the nominally axisymmetric sensors. This suggests that additional work be conducted to address the ability to maintain plasma wall gap when the axisymmetric flux loop signals are being modified through 3D plasma effects. The problem appears to become worse in

H-mode as the axisymmetric flux loop response to 3D fields becomes large. This may be alleviated in part by B-field measurements which can allows differentiation between 2D and 3D effects. Additionally, validation of models through comparison of measured and simulated 3D magnetic diagnostic response is an ongoing work [23]. Future work includes 2D equilibrium reconstruction using 3D predicted fields to asses the full impact of such control assumptions.

As a final commentary on this work, the profiles generated by the CORSICA code, and utilized in the VMEC calculations, did not include any profile modifications due to RMP application. The results here are considered approximate. Still, this work highlights the ability to asses the effect of RMPs on the ITER plasma and diagnostics using modern 3D equilibrium tools.

Acknowledgments

[1] S. P. Hirshman and J. C. Whitson. Steepest-descent moment method for three-dimensional magnetohydrodynamic equilibria. *Phys. Fluids*, 26(12):3553–3568, 1983.

[2] R.J. Hawryluk, D.J. Campbell, G. Janeschitz, P.R. Thomas, R. Albanese, R. Ambrosino, C. Bachmann, L. Baylor, M. Becoulet, I. Benfatto, J. Bialek, A. Boozer, A. Brooks, R. Budny, T. Casper, M. Cavinato, J.-J. Cordier, V. Chuyanov, E. Doyle, T. Evans, G. Federici, M. Fenstermacher, H. Fujieda, K. G'al, A. Garofalo, L. Garzotti, D. Gates, Y. Gribov, P. Heitzenroeder, T.C. Hender, N. Holtkamp, D. Humphreys, I. Hutchinson, K. Ioki, J. Johner, G. Johnson, Y. Kamada, A. Kavin, C. Kessel, R. Khayrutdinov, G. Kramer, A. Kukushkin, K. Lackner, I. Landman, P. Lang, Y. Liang, J. Linke, B. Lipschultz, A. Loarte, G.D. Loesser, C. Lowry, T. Luce, V. Lukash, S. Maruyama, M. Mattei, J. Menard, M. Merola, A. Mineev, N. Mitchell, E. Nardon, R. Nazikian, B. Nelson, C. Neumeyer, J.-K. Park, R. Pearce, R.A. Pitts, A. Polevoi, A. Portone, M. Okabayashi, P.H. Rebut, V. Riccardo, J. Roth, S. Sabbagh, G. Saibene, G. Sannazzaro, M. Schaffer, M. Shimada, A. Sen, A. Sips, C.H. Skinner, P. Snyder, R. Stambaugh, E. Strait, M. Sugihara, E. Tsitrone, J. Urano, M. Valovic, M. Wade, J. Wesley, R. White, D.G. Whyte, S. Wu, M. Wykes, and L. Zakharov. Principal physics developments evaluated in the iter design review. *Nuclear Fusion*, 49(6):065012, 2009.

[3] M. Becoulet, F. Orain, P. Maget, N. Mellet, X. Garbet, E. Nardon, G.T.A. Huysmans, T. Casper, A. Loarte, P. Cahyna, A. Smolyakov, F.L. Waelbroeck, M. Schaffer, T. Evans, Y. Liang, O. Schmitz, M. Beurskens, V. Rozhansky, and E. Kaveeva. Screening of resonant magnetic perturbations by flows in tokamaks. *Nuclear Fusion*, 52(5):054003, 2012.

[4] T.E. Evans, D.M. Orlov, A. Wingen, W. Wu, A. Loarte, T.A. Casper, O. Schmitz, G. Saibene, M.J. Schaffer, and E. Daly. 3d vacuum magnetic field modelling of the iter elm control coil during standard operating scenarios. *Nuclear Fusion*, 53(9):093029, 2013.

[5] Samuel Lazerson and Ian T Chapman. STELLOPT modeling of the 3D diagnostic response in ITER. *Plasma Physics and Controlled Fusion*, 55(8):084004, 2013.

[6] G. Vayakis. Personal Communication, 2013.

[7] T Casper, Y Gribov, A Kavin, V Lukash, R Khayrutdinov, H Fujieda, C Kessel, ITER Organization, and ITER Domestic Agencies. Development of the ITER baseline inductive scenario. *Nuclear Fusion*, 54(1):013005, December 2013.

[8] J. A. Crotinger, L. LoDestro, L. D. Pearlstein, A. Tarditi, T. A. Casper, and E. B. Hooper.

Corsica: A comprehensive simulation of toroidal magnetic-fusion devices. Technical Report UCRL-ID-126284, Lawrence Livermore National Laboratory, Apr 1997.

[9] D.A. Spong, S.P Hirshman, L.A. Berry, J.F. Lyon, R.H. Fowler, D.J. Strickler, M.J. Cole, B.N. Nelson, D.E. Williamson, A.S. Ware, D. Alban, R. Sànchez, G.Y. Fu, D.A. Monticello, W.H. Miner, and P.M. Valanju. Physics issues of compact drift optimized stellarators. *Nucl. Fusion*, 41:711–716, 2001.

[10] Y. Gribov. Personal Communication, 2013.

[11] M J Schaffer, J E Menard, M P Aldan, J M Bialek, T E Evans, and R A Moyer. Study of in-vessel nonaxisymmetric ELM suppression coil concepts for ITER. *Nuclear Fusion*, 48(2):024004, January 2008.

[12] Y Gribov and A Loarte. Currents in elm coils for edge plasma shape perturbation studies. Technical Report 98BA5X, ITER Organization, June 2012.

[13] S A Lazerson, S Sakakibara, and Y Suzuki. A magnetic diagnostic code for 3d fusion equilibria. *Plasma Physics and Controlled Fusion*, 55(2):025014, 2013.

[14] S A Lazerson. The virtual-casing principle for 3d toroidal systems. *Plasma Physics and Controlled Fusion*, 54(12):122002, 2012.

[15] V.D. Shafranov and L.E. Zakharov. Use of the virtual-casing principle in calculating the containing magnetic field in toroidal plasma systems. *Nucl. Fusion*, 12:599–601, 1972.

[16] J.D. Hanson and S.P. Hirshman. Compact expressions for the biot-savart fields of a filamentary segment. *Phys. of Plasmas*, 9(10):4410–4412, 2002.

[17] M C Zarnstorff, A Weller, Joachim Geiger, E Fredrickson, Stuart R Hudson, J Knauer, Allan H Reiman, A Dinklage, G Y Fu, and L P Ku. Equilibrium and stability of high-beta plasmas in wendelstein 7-as. In *proceedings of the 20th IAEA Fusion Energy Conference*, pages EX/3–4, November 2004.

[18] Samuel Lazerson, David A Gates, D Monticello, G H Neilson, N Pomphrey, Allan H Reiman, Satoru Sakakibara, and Yasuhiro Suzuki. Equilibrium Reconstruction on the Large Helical Device. In *38th EPS Conference on Plasma Physics*, pages 1–4, July 2011.

[19] Samuel Lazerson, Joachim Geiger, Yuri Gribov, Stuart Hudson, and David Gates. Applications of 3d equilibrium reconstruction. *Bulletin of the American Physical Society*, 58, 2013.

[20] Todd E Evans, Richard A Moyer, Keith H Burrell, Max E Fenstermacher, Ilon Joseph, Anthony W Leonard, Thomas H Osborne, Gary D Porter, Michael J Schaffer, Philip B Snyder, Paul R Thomas, Jonathan G Watkins, and William P West. Edge stability and transport control with resonant magnetic perturbations in collisionless tokamak plasmas. *Nature Physics*, 2(6):419–423, May 2006.

[21] M F Heyn, I B Ivanov, S V Kasilov, W Kernbichler, A Loarte, V V Nemov, and A M Runov. On the confinement of passing alpha particles in a tokamak-reactor with resonant magnetic field perturbations shielded by plasma currents. *Nuclear Fusion*, 52(5):054010, May 2012.

[22] A D Turnbull, N M Ferraro, V A Izzo, Edward A Lazarus, J K Park, W A Cooper, Steven P Hirshman, Lang L Lao, M J Lanctot, Samuel Lazerson, Y Q Liu, Allan H Reiman, and F Turco. Comparisons of linear and nonlinear plasma response models for non-axisymmetric perturbations. *Physics of Plasmas*, 20(5):056114, 2013.

[23] J. D. King, E. J. Strait, R. L. Boivin, R. J. La Haye, L. L. Lao, D. J. Battaglia, N. C. Logan, J. M. Hanson, M. J. Lanctot, and A. C. Sontag. Design of a 3D Magnetic Diagnostic System for DIII-D. In *APS Meeting Abstracts*, page 8108P, October 2012.